Astron. Astrophys. 342, 453–463 (1999)

ASTRONOMY AND ASTROPHYSICS

# Line-profile variations due to adiabatic non-radial pulsations in rotating stars

## IV. The effects of intrinsic profile variations on the IPS diagnostics

**C. Schrijvers**[1] **and J.H. Telting**[2]

[1] Astronomical Institute Anton Pannekoek, University of Amsterdam, and Center for High Energy Astrophysics, Kruislaan 403, 1098 SJ Amsterdam, The Netherlands
[2] Isaac Newton Group of Telescopes, ASTRON/NFRA, Apartado 321, E-38780 Santa Cruz de La Palma, Spain

Received 14 August 1998 / Accepted 20 October 1998

**Abstract.** We calculate time series of Doppler-broadened line-profiles of rotating stars that exhibit non-radial pulsations. We investigate the variability of such line profiles for cases in which variations of the intrinsic line-profile cannot be neglected. To study the effects of atmospheric changes on the line-profile variability we include: (1) local changes of the surface brightness, (2) local changes in the equivalent width of the intrinsic line profile, and (3) a non-adiabatic phase lag between the radial pulsational displacement and the surface-temperature perturbations.

We parameterize these three effects to extend the study presented in Paper I. The variability is analyzed by means of amplitude and phase diagrams obtained from Fourier transforms at each point of the line profile. One of our findings is that an asymmetry in the distribution of amplitude across the line profile can be caused by non-adiabaticity of the contributing temperature variations.

We perform Monte-Carlo simulations to investigate the correlation between the phase diagrams and the $\ell$ and $m$ values of modes, in cases with line-profile variability that is dominated by the variable atmospheric properties. The retrieval of $\ell$ turns out to be similarly successful as in Paper II, where the variability was dominated by the surface-velocity field. We also find that harmonic variability is specific for pulsational surface-velocity fields rather than for variations of the surface temperature.

**Key words:** line: profiles – methods: data analysis – stars: early-type – stars: oscillations – stars: rotation – stars: variables: $\delta$ sct

### 1. Introduction

The study of stellar pulsations provides one of the few observational tests for theoretical models of stellar structure and evolution. Asteroseismology aims to constrain the internal structure of an observed star by comparing identified pulsation modes with a theoretical model. A promising tool for such identifications is the analysis of time series of photospheric absorption line profiles. With the advanced status of modern spectroscopy the observed characteristics of multi-periodic pulsating stars should provide sufficient information for asteroseismological purposes. The success of such an approach depends on the ability to retrieve the correct pulsation parameters.

Non-radial pulsations (NRP) divide the stellar surface in regions with different velocity fields and temperatures. The velocity fields give rise to local Doppler shifts. The temperature variations cause local brightness and equivalent width changes. Due to the rotation of the star these variations are Doppler mapped to the absorption line profiles, typically creating a moving pattern of peaks and troughs.

In many studies concerning the variations of stellar line profiles caused by NRP, the Doppler redistribution of flux by the oscillatory surface velocity field is assumed to be mainly responsible for the variations. In theoretical studies (e.g. Kambe & Osaki 1988, Kennelly et al. 1992, Aerts & Waelkens 1993, Hao 1998) as well as those concerning observed line-profile variations of pulsating stars (e.g. Smith 1977, Vogt and Penrod 1983, Baade 1984, Gies & Kullavaijana 1988, Kambe et al. 1990) the contribution of atmospheric changes caused by the pulsation is often neglected, i.e. the intrinsic line profile is assumed constant over the stellar surface. Few applications of variable intrinsic line profiles in models are known (Balona 1987, Gies 1991, Lee et al. 1992, Townsend 1997). These works demonstrate that these effects can be important to include in analyses.

In a previous paper (Schrijvers et al. 1997, hereafter Paper I) we synthesized line-profile variations solely caused by Doppler-redistribution of flux due to the surface velocities of an adiabatically pulsating rotating star, neglecting all other effects of the pulsation. The variability was then analyzed by means of a diagnostic called the Intensity Period Search method (IPS method). We found that a number of the important NRP parameters are reflected by the IPS diagnostics in a typical or even unique way, which allows retrieval of some of them.

In general, the line-profile variations of non-radially pulsating stars are affected by periodic changes in the physical prop-

*Correspondence to*: coen@astro.uva.nl

erties of the atmosphere as well, notably by variations of surface temperature and gravity. Here, we extend our study of Paper I, by investigating the effects of local atmospheric brightness and equivalent width (EW) variations on the IPS diagnostics. We refer to local variations of brightness and EW as $T$-effects, and to effects of surface-velocity fields as $V$-effects. We will show that most of the conclusions of Paper I also apply to the more general case. In addition, we will illustrate effects which are typical for line-profile variability arising from $T$-effects. We also address effects that we find to be typical for a combination of $T$-effects and $V$-effects.

The presently introduced model for the pulsation-related changes in the intrinsic line profile was already applied in Telting and Schrijvers (1997, hereafter Paper II). In that paper we investigated cases for which $V$-effects dominate the $T$-effects. From Monte-Carlo simulations we showed that the maximum blue-to-red phase difference at the main frequency is an indicator of the $\ell$-value of the pulsation mode. In addition, the maximum blue-to-red phase difference at the first harmonic frequency, if detected, can be used to determine the $|m|$-value of the pulsation mode. Here we perform similar Monte-Carlo simulations, but for cases in which the $T$-effects dominate over the $V$-effects.

In Sect. 2 we define the model for the local intrinsic line profile, and specify the domains that we explore for the three temperature-related parameters. Sect. 3 summarizes our method of analysis and explains the diagnostic IPS diagrams which we use to characterize the line-profile variability. In Sect. 4 we generate time-series of line profiles for various combinations of parameters and calculate the corresponding IPS diagrams, and discuss the effects of the local variations of the intrinsic line profile on the IPS diagnostics. In Sect. 5 we present Monte-Carlo simulations of phase diagrams for line-profile variability that is dominated by pulsation-related temperature perturbations. We summarize our conclusions in Sect. 6.

## 2. The effects of pulsationally induced atmospheric variations on the intrinsic line profile

In practice, the local surface brightness and local intrinsic line profile are complex functions of the physical properties of the star. In this work, we do not aim at accounting for the physics of the atmosphere in a sophisticated way. This would require detailed model atmospheres that apply to specific situations. Our goal is rather to investigate the effects of local variations of the surface brightness and intrinsic line profile on the characteristics of the line-profile variability in general. Therefore, we use simplified descriptions of the perturbed surface brightness and intrinsic line profile, which depend only on the modeled surface temperature.

We incorporate the effects of local variations of the intrinsic line profile in a simple and parameterized way. We account for local brightness and EW changes which are induced by the local oscillatory changes of the atmosphere, in a similar way as Lee et al. (1992). Furthermore, we allow for a non-adiabatic phase lag between the displacement field of the pulsation and the pulsational surface-temperature variations. Our expressions of the Lagrangian displacement field, including the terms which account for the effects of the Coriolis force, are given in Paper I.

### 2.1. Perturbations of the surface temperature

We assume a linear relation between the perturbations in surface temperature and the radial component of the Lagrangian displacement field:

$$\frac{\delta T}{T} \propto Y_\ell^m\left(\theta,\phi\right) e^{\mathrm{i}(\omega t+\chi)} \ , \tag{1}$$

where the symbols $\ell$, $m$, $Y_\ell^m\left(\theta,\phi\right)$, $\omega$ and $t$ have their usual meaning (see Paper I). The amplitude of the surface temperature variation $\delta T/T$ is specified by the parameter: $(\delta T/T)_{\max}$. In all our calculations, we choose a value for $(\delta T/T)_{\max}$ within the domain $[0.0, 0.1]$, i.e. for each mode we allow variations in temperature up to 10% of the surface temperature of the star (20% peak-to-peak).

In the adiabatic limit, the local temperature variation is in phase with the radial displacements for $g$ modes, while it is in anti-phase for $p$ modes. In the non-adiabatic case, an additional phase lag can be present (Stellingwerf 1978, Saio & Cox 1980, Cugier et al. 1994). Our description of the surface velocity field is based on an adiabatic treatment of the pulsation. Nevertheless we introduce a non-adiabatic phase lag between the surface temperature and the radial displacement field. This allows us to investigate what types of behavior might be expected for non-adiabatic modes. We define the phase difference between the radial (vertical) displacement and the local temperature variation by

$$\chi = \chi_{k,\ell}^{\mathrm{a}} + \chi^{\mathrm{na}} \ , \tag{2}$$

where $\chi_{k,\ell}^{\mathrm{a}}$ is the phase difference in the limit of adiabaticity and $\chi^{\mathrm{na}}$ is the non-adiabatic component of the phase of temperature variation. For the adiabatic phase difference we use $\chi_{k,\ell}^{\mathrm{a}} = 180^\circ$ for $p$ modes, and $\chi_{k,\ell}^{\mathrm{a}} = 0^\circ$ for $g$ modes.

We use a sharp distinction between $p$ modes and $g$ modes based on $k$, the ratio of the horizontal to the vertical displacement amplitude. To discriminate between $p$ modes ($k < K$) and $g$ modes ($k > K$), we use the positive root of the equation

$$\ell(\ell+1)K^2 - 4K - 1 = 0 \tag{3}$$

(Buta and Smith 1979). Although modes with intermediate values of $k$ may in reality be a complex mixture of $p$ mode and $g$ mode type oscillation, the equation of Buta and Smith is well suited for our purposes.

Calculations of phase lags of the temperature perturbation, with a linear nonadiabatic oscillation model, are performed by Cugier et al. (1994). For various oscillation parameters and different $\beta$ Cephei models they calculate the phase of the temperature perturbations. They find values up to $35^\circ$ for $\ell \leq 2$. We treat the non-adiabatic lag $\chi^{\mathrm{na}}$ as a free parameter, allowing values between $-45^\circ$ and $45^\circ$ for all $\ell$-values.

### *2.2. Parameterization of the local changes in brightness and equivalent width*

At this point we have a parameterized description of the perturbations of both surface velocities (Paper I) and surface temperatures due to non-radial pulsations. The effect of velocity fields on the line-profile formation is relatively easy to understand as wavelength shifts of the local intrinsic line profiles according to the velocity component in the line of sight. However, the implications of local changes of the surface temperature on the line formation are much more complex. The physics of radiative transfer, associated with this issue, depends on the detailed properties of the star. In spite of this complexity in specific cases, the general picture of the effect of a change in local temperature on the line-profile formation can be approximated by changes of the local surface brightness and the line strength (and shape) of the intrinsic line profile.

To circumvent the complex problems of radiative transfer, and hence avoiding too many additional parameters, we introduce a parameterization of the changes in surface brightness and line strength which is easy to implement and which introduces a minimum number of new parameters to the model. We define our intrinsic line profile as a function of radial velocity, $V$, centered around $V_0$

$$f_{\rm intr}(V,T) = \mathcal{I}(T)\left(1 - \frac{W_{\rm E,intr}(T)}{W\sqrt{\pi}}{\rm e}^{-((V-V_0)/W)^2}\right) , \quad (4)$$

where $W$ is the width of the intrinsic profile. The functions $\mathcal{I}(T)$ and $W_{\rm E,intr}(T)$ specify the temperature dependence of the local surface brightness and local EW, respectively. These two functions of the local surface temperature will be defined by Eqs. (5) and (6) below. The function given in Eq. (4) is essentially the same Gaussian as used in Paper I, but with the surface brightness and EW now depending on the surface temperature $T$.

#### 2.2.1. Local brightness variations

Our model for the Lagrangian displacement field applies to relatively small displacements ($\xi_r/R << 1$). A linear approximation of the local surface brightness is therefore adequate for our purposes. We define the linear relation between the perturbations of the local surface-brightness and surface temperature by

$$\frac{\delta\mathcal{I}}{\mathcal{I}} = 1.8\frac{\delta T}{T} \quad (5)$$

The coefficient with a value of $1.8$ (see Paper II) follows from the evaluation of the temperature derivative of the optical continuum fluxes $F_\lambda$ of stars hotter than approximately $10^4$K, given by Kurucz (1992).

The temperature-independent local intensity $\mathcal{I}_0$ is determined by a linear limb-darkening approximation which is given in Paper I. Again, we adopt a limb-darkening coefficient $\alpha = 0.35$, which is appropriate for early B-type stars in the optical region (Wade & Rucinski 1985).

#### 2.2.2. Local changes of the intrinsic equivalent width

We change the EW of the local intrinsic line profile ($W_{\rm E,intr}$) by changing only the depth of the profile (see Eq. (4)). It is not important whether the changes in EW are represented by changes in line width or line depth, as long as the rotation is the dominant broadening mechanism. For the perturbations of the local EW, we take the following dependence on the surface-temperature variation

$$\frac{\delta W_{\rm E,intr}}{W_{\rm E,intr}} = \alpha_{W_{\rm E}}\frac{\delta T}{T} . \quad (6)$$

The coefficient $\alpha_{W_{\rm E}}$, which we call the EW-response, is the third free parameter added to the model. It can be positive or negative.

A similar implementation of the pulsationally induced changes of the intrinsic line profile was used by Lee et al. (1992). They used theoretical LTE and non-LTE equivalent widths for Si III and He I lines to illustrate that a wide range of values of $\alpha_{W_{\rm E}}$ can be expected for different spectral lines and different effective surface temperatures. They calculated line profiles for carefully selected combinations of their model parameters, illustrating the typical line-profile behavior which can be expected from NRP-related temperature variations.

We limit our calculations to the interval $\alpha_{W_{\rm E}} \epsilon [-4, 2]$. Given the allowed range for the amplitude of the variations of the local temperature (amplitudes less than $10\%$), the local change in EW will always be less than $40\%$. As with all our other parameters, the interval for $\alpha_{W_{\rm E}}$ is chosen to display all possible interactions with the brightness variations and surface-velocity fields. Values for $\alpha_{W_{\rm E}}$ outside the above interval are expected. In practice, the aspects illustrated for the extreme values are likely to be also representative for cases outside this interval, because the trend continues outside our considered range (see Fig. 3).

## 3. Analysis of the time series by means of IPS diagnostics

We calculate amplitude and phase diagrams as diagnostic tools for studying line-profile variations. The diagrams are equivalent to the power and phase diagrams obtained from a Fourier analysis as proposed by Gies & Kullavanijaya (1988).

The apparent frequency of observed line-profile variability ($\omega_{\rm obs}$) has to be determined by Fourier techniques. Since the intensity variations in the line profile are not strictly sinusoidal (see Gies 1991 and Paper I), there will also be some variational power distributed over harmonics. Once the main frequency is known, the variability of the normalized intensity can be decomposed into its harmonic contributions, which is in our case conveniently achieved by fitting a combination of sinusoids of the form

$$\begin{aligned}\Delta I(V,t) &= I_0(V)\sin(\omega_{\rm obs}t + \Psi_0(V)) \\ &+ I_1(V)\sin(2\omega_{\rm obs}t + \Psi_1(V)) \end{aligned} \quad (7)$$

to the intensity variations in each velocity bin of a time series of generated spectra.

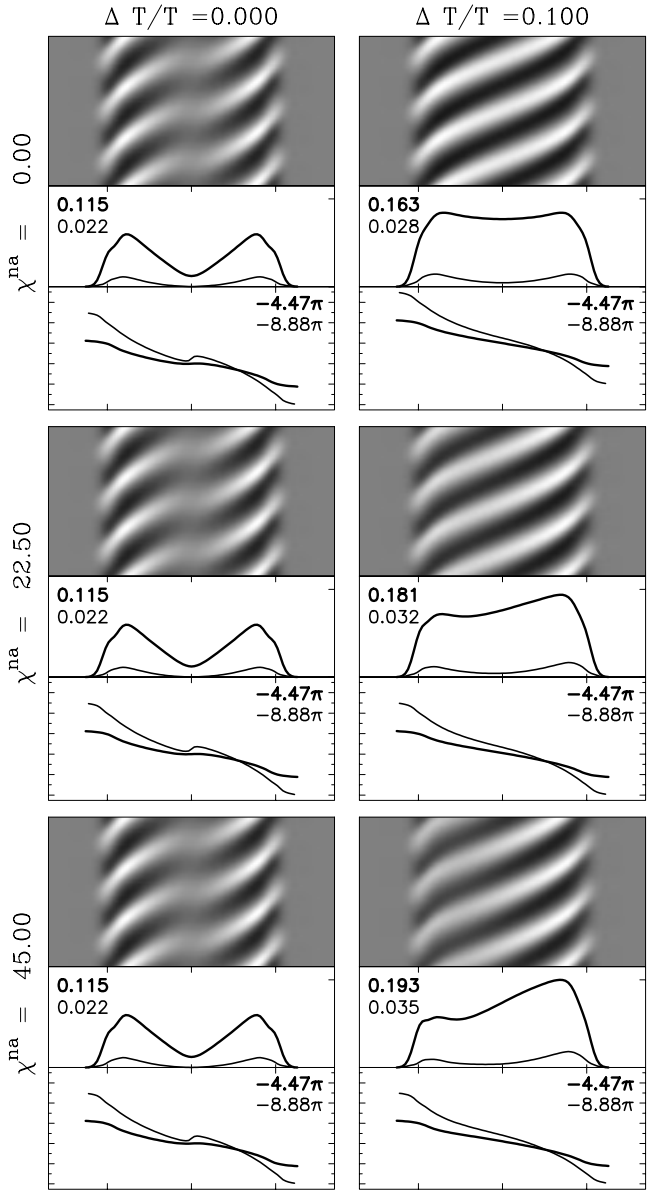


**Fig. 1.** Effects of phase lag and temperature amplitude. Residual spectra (*upper*, grey scale) amplitude (*middle*) and phase (*lower*) distributions of time series of line profiles for varying values of $(\delta T/T)_{\max}$ and $\chi^{\rm na}$. The other relevant parameters are: $\alpha_{W_{\rm E}}$=+1, $\ell$=5, $m$=−5, $V_{\max}$=0.07$V_{\rm e}\sin i$, $k^{(0)}$=1.0, $i$=70°, $\Omega/\omega^{(0)}$=0.0, $W$=0.10$V_{\rm e}\sin i$. Thick lines indicate the amplitude and phase diagrams corresponding to the main frequency. Thin lines correspond to the first harmonic frequency. The horizontal tick marks indicate $V_{\rm e}\sin i$. The vertical large tick marks in the phase diagram indicate $2\pi$. A detailed description of the diagrams is given in Sect. 3

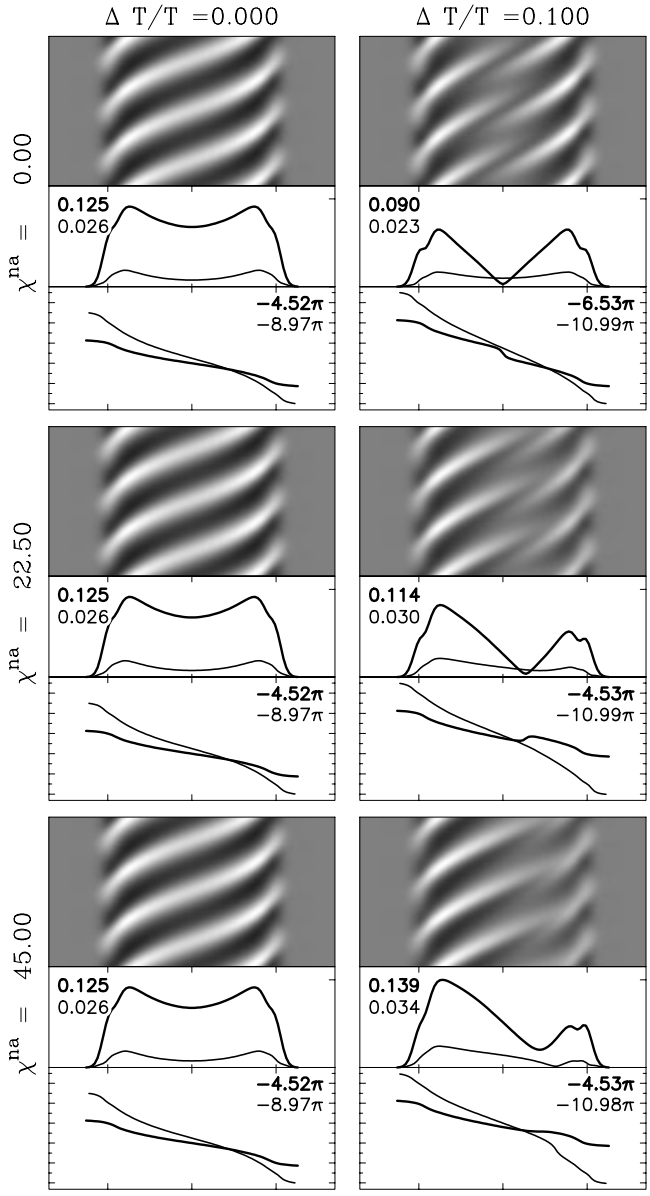


**Fig. 2.** Similar to Fig. 1, but for $\alpha_{W_{\rm E}}=-4$ and $k^{(0)}$=0.3

For the apparent frequency and its harmonic, we calculate the amplitudes ($I_0$, $I_1$) and phases ($\Psi_0$, $\Psi_1$) for each position in the line profile. We remove the $2\pi$ wrap from $\Psi_0$ and $\Psi_1$ to create continuous blue-to-red phase diagrams.

In Figs. 1, 2 and 3 we show the amplitude and phase diagrams (IPS diagnostics) to illustrate the characteristic behavior of the diagnostic diagrams as a function of the temperature-related parameters. The individual diagrams in these figures consist of three panels. Three pulsation cycles of residual (mean subtracted) spectra are shown as dynamic spectra in a grey-scale image (top panel). Intensities less than average are indicated darker and bright regions in the profile are indicated by lighter shades. In the middle panel we plot the amplitude distributions at the main frequency $I_0(V)$ (thick line) and its harmonic $I_1(V)$ (thin line). The maximum values of the two amplitude distributions are given in units of the average central line depth ($d_{\rm mean}$). The thick and thin lines in the bottom panel display the corresponding phase diagrams $\Psi_0(V)$ and $\Psi_1(V)$, respectively. The maximum phase differences of both diagrams $\Delta\Psi_0$ and $\Delta\Psi_1$ are given inside the bottom panel, in radians.

A more detailed description of our implementation of the method and diagrams is given in Paper I.

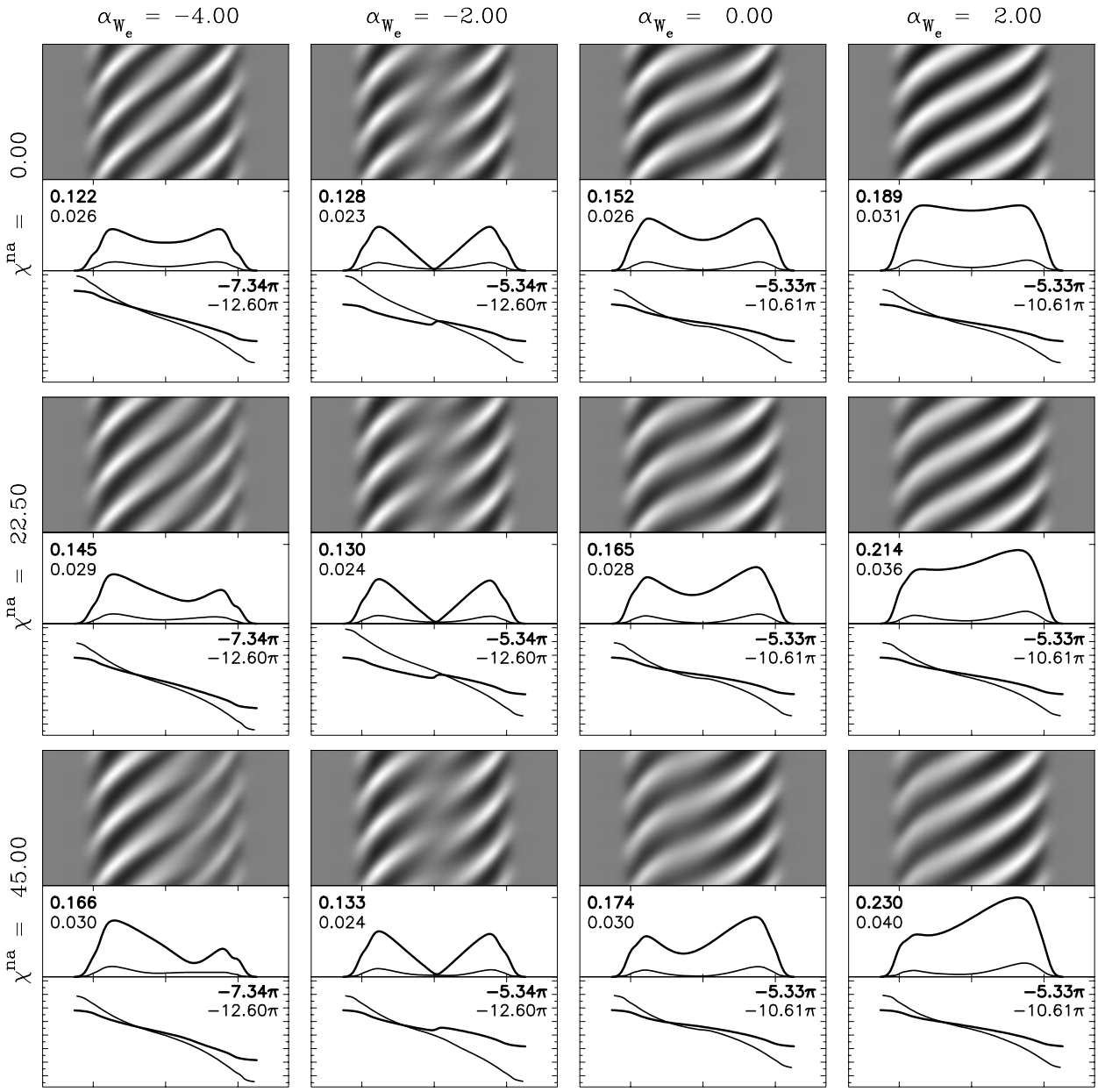


**Fig. 3.** Effects of EW response and phase lag. Similar to Fig. 1, but for varying values of $\chi^{\rm na}$ and $\alpha_{W_{\rm E}}$. The other relevant parameters are: $(\delta T/T)_{\rm max} = 0.10$, $\ell = 6$, $m = -6$, $V_{\rm max} = 0.07 V_{\rm e} \sin i$, $k^{(0)} = 2.00$, $i = 80^\circ$, $\Omega/\omega^{(0)} = 0.0$, $W = 0.10 V_{\rm e} \sin i$

## 4. The effects of local changes in brightness and EW on the IPS diagnostics

We calculate time series of line profiles and the corresponding IPS diagnostics for subsets of parameter space. Special attention is given to the three parameters which specify the $T$-effects. Figs. 1, 2 and 3 are examples of such calculations.

We find, in accordance with Lee et al. (1992), that the modeled variations in either brightness or EW lead to comparable effects in the line-profile variability. This can be understood by considering that areas on the stellar surface with an increased brightness as well as areas of increased intrinsic EW both lead to an increased absorption at the corresponding position in the line profile. The effect of EW variations may work either cooperatively or destructively with the effect of brightness variations. For modes with $\ell$-values larger than 3 and $\alpha_{W_{\rm E}} \approx -1.8$, we find that both effects cancel almost completely for our model (see Fig 3, second column).

The fact that we find such cancellation at values of $|\alpha_{W_{\rm E}}|$ close to 1.8, which is also the value of the coefficient that we use in Eq. (5), is not a coincidence. Since the brightness and EW variations have very similar effects on the line-profile variability, both effects act almost exactly opposite at $\alpha_{W_{\rm E}} \approx -1.8$. In the next sections we will refer to $\alpha_{W_{\rm E}} \approx -1.8$ as the boundary between the cooperative and destructive nature of the EW effect. Note that this boundary value depends on the coefficient

used in Eq. (5), for which we took a value suitable for $\beta$ Cephei stars. So for a coefficient of 4 in Eq. (5) (which may be a better approximation for $\delta$ Scuti stars), we would find a 'boundary' at $\alpha_{W_{\rm E}} \approx -4$.

We elaborate on the cooperativeness and/or destructiveness between local brightness and EW effects in Sect. 4.2.

### *4.1. $k$-characteristics of IPS amplitude diagrams*

The typical double-peaked shape of the IPS amplitude diagrams at the input frequency which are found (e.g. Paper I) for velocity-dominated line-profile variations of modes with high $k$ values ($g$ modes) may vanish completely for $\alpha_{W_{\rm E}} \gtrsim -1.8$, if the relative importance of $T$-effects is large enough (see e.g. Fig. 1). In such cases we cannot distinguish between low and high values of $k$ based on the variations at the input frequency. This confirms the results of Lee et al. (1992) who showed that $T$-effects may lead to dominant variations in the line center.

In contrast, if $\alpha_{W_{\rm E}} \lesssim -1.8$ we find the reverse effects for modes having $k$ close to but greater than $K$ (see Eq. 3). In such cases the $T$-effects may *remove* power around the line center leading to a double-peaked amplitude distribution (instead of a rectangular shaped distribution, which is typical for these modes). This effect is illustrated in Fig. 2. Our conclusion in Paper I, stating that only cases with a double-peaked amplitude distribution give unambiguous information by explicitly implying a high $k$-value, is therefore not valid for the generalized model that includes $T$-effects: it only applies to absorption lines for which $\alpha_{W_{\rm E}} \gtrsim -1.8$.

In case of brightness variations only (i.e. if EW is kept constant), we find for $g$ modes that the total power of the variations at the input frequency is enhanced, but that the total power is reduced by the brightness variations associated with $p$ modes. This difference in behavior results from the differing adiabatic phase difference $\chi^{\rm a}_{k,\ell}$ of $p$ and $g$ modes (see Sect. 2.1).

While amplitude diagrams at the input frequency may be completely changed by temperature effects, the double-peaked shape of the amplitude distributions at the first harmonic frequency are not. We find that the $T$-effects do not give rise to large changes of the harmonic variability, leaving the typical harmonic amplitude distribution arising from the $V$-effects unaffected.

### *4.2. Asymmetry in IPS amplitude diagrams*

We find asymmetries in the IPS amplitude diagrams if we allow a non-adiabatic phase lag (see Figs. 1, 2 and 3). For isolated lines, asymmetric amplitude diagrams appear only if both the surface velocities and $T$-effects of a non-adiabatic mode contribute significantly. We find large asymmetries for $|\chi^{\rm na}| \gtrsim 10^\circ$.

These asymmetries can be understood by considering that, for example, the surface areas approaching the observer (in the corotating frame) are brighter than those moving away. In such a case the blue-shifted intrinsic profiles systematically contribute more to the observed line-profile variations than the red-shifted intrinsic profiles do, leading to variability more pronounced in the blue part of the observed line profile than in the red part. We find that the centroid of the asymmetric IPS amplitude distribution is shifted either redwards or bluewards, depending on the combined effect of the EW response $\alpha_{W_{\rm E}}$ and the total phase lag $\chi$. This is illustrated in Fig. 3.

For only brightness variations (constant EW) we find that $g$ modes with $\chi^{\rm na} > 0$ and $p$ modes with $\chi^{\rm na} < 0$ give rise to a red-shifted centroid of the amplitude diagram, whereas $g$ modes with $\chi^{\rm na} < 0$ and $p$ modes with $\chi^{\rm na} > 0$ lead to a centroid shifted towards the blue wing. The local EW variations show similar behavior if $\alpha_{W_{\rm E}} > 0$, which enhances the above-mentioned asymmetry even more. However, if $\alpha_{W_{\rm E}} < 0$ the EW variations give rise to an effect opposite to that of the brightness variations. As mentioned before, the destructive effects of brightness and EW variations will lead to an almost complete disappearance (if $\ell > 3$) of the $T$-effects for $\alpha_{W_{\rm E}} \approx -1.8$. For $\alpha_{W_{\rm E}} \lesssim -1.8$ the shift of the centroid is reversed. Time-series of spectra that consist of more than one spectral line may therefore have opposite shifts of the centroids of the amplitude distributions of different lines (if some of the lines have $\alpha_{W_{\rm E}} \lesssim -1.8$).

### *4.3. Discrete phase jumps caused by $T$-effects*

When combined with pulsational velocity fields the $T$-effects can lead to $2\pi$ differences in phase, similar to the $2\pi$ differences in cases of a high value for $k$ as discussed in Paper I (Sect. 6.1.2). This is illustrated in Fig. 3, where the large negative response of the local EW connects the phases in the blue and red half of the diagram in a different way as the brightness variations do. In this example it leads to a $2\pi$ change in the total phase difference at the main frequency for the phase diagrams in the left column as compared to the three other columns in the figure. A similar effect is present for the total phase difference at the first harmonic, as illustrated by the two left columns in Fig. 3.

### *4.4. Variability at harmonic frequencies: $T$ versus $V$-effects*

For our model we find that variability at the harmonic frequencies is a characteristic of line-profile variations dominated by pulsational surface velocities. Line-profile variability from brightness variations alone shows no harmonic variability at all. In cases with large variations in EW we find very small harmonic amplitudes. However, these are only significant in cases when variations at the input frequency are very large ($> 20\%$ of $d_{\rm mean}$, where $d_{\rm mean}$ is the average central line-depth). For a fixed line-profile amplitude the ratio of the amplitude at the first harmonic to that at the input frequency ($A_1/A_0$), is much larger for variability arising from surface-velocity variations than for variability from local EW variations. Within our ranges of temperature amplitude and EW-response we are not able to create the non-sinusoidal line-profile variations (i.e. significant harmonic amplitude) typical for the variations arising from surface-velocity fields. Note that the harmonic variability in the time series of Figs. 1, 2 and 3 is mainly caused by the additional velocity fields that were allowed, whereas the variation at the input frequency is dominated by the $T$-effects.

We tested the specific sensitivities of the IPS phase diagrams to the individual mechanisms ($T$-effects and $V$-effects) responsible for the line-profile variability (see Figs. 1, 2 and 3, and Figs. 3-9 in Paper I). Within the given parameter ranges the blue-to-red phase differences from line-profile variations caused by $T$-effects show a behavior which is not different from what we find for the variability only caused by surface velocities. In all cases $\Delta\Psi_0$ and $\Delta\Psi_1$ appear to be related to $\ell$ and $m$ respectively. We elaborate on this in Sect. 5.

The key feature to discriminate between $V$- and $T$-effects is the presence (or absence) of a harmonic. The presence of a harmonic component in the line-profile variations indicates that the variability is, at least partly, caused by $V$-effects. Line-profile variations caused by $T$-effects are nearly sinusoidal, giving rise to harmonics which are too small to be detected (see also Sect. 5.1). For line-profile variations with small amplitudes (of the order of $1\%$ of $d_{\rm mean}$) absence of harmonic variability does not necessarily indicate $T$-effects, since for small amplitudes a harmonic is expected for neither $V$-effects or $T$-effects. If, however, the amplitude is rather large (of the order of $10\%$ of $d_{\rm mean}$) the absence of a harmonic clearly indicates the dominance of $T$-effects, since large variations caused by $V$-effects are expected to have a significant harmonic component.

The non-sinusoidal nature of the variations can sometimes be detected directly from the profiles themselves (if a single mode dominates). Non-sinusoidal temporal variations in the time series are always accompanied by a non-sinusoidal behavior in the spatial direction of the individual residual line profiles: the quasi-emission bumps appear broad and shallow while the quasi-absorption peaks appear narrow and deep.

An example of such a case in which we expect large harmonic variability is the $\beta$ Cephei star $\omega^1$ Sco (Telting & Schrijvers 1998). In spite of insufficient temporal sampling of the data, which hampered the detection of a harmonic, the broad and shallow bumps and narrow and deep peaks in the line profiles of $\omega^1$ Sco indicate that the variability has a dominant contribution from surface-velocity effects.

## 5. Monte-Carlo simulations of IPS phase diagrams for temperature-dominated line-profile variability

In our previous papers we investigated the diagnostics derived by the IPS method for line-profile variability from velocity-dominated nonradial pulsations. In Paper I we show evidence for the relations between the observables $\Delta\Psi_0$ and $\Delta\Psi_1$, and the pulsation indices $\ell$ and $|m|$ respectively. These relations were established in Paper II, where we presented a method to retrieve $\ell$ and $|m|$ from observed time series of spectra. In these papers the generated variability was mainly due to the surface-velocity fields of the nonradial pulsation.

Here we investigate the total phase differences at the main and first harmonic frequency for cases in which the line-profile variability is completely or predominantly caused by $T$-effects. We determine relations similar to those in Paper II (see Eq. (8) therein). Also, we investigate the differences between line-profile variability caused by pulsational velocity-fields and $T$-variations.

**Table 1.** Simulation 1. Parameter ranges in a Monte-Carlo simulation for our sample with $T$-effects only. Since $V_{\rm max} = 0$, the parameters $k^{(0)}$, $\Omega/\omega^{(0)}$ and $\chi^{\rm na}$ are not relevant

| | | | |
|---|---|---|---|
| $\ell$ | 0 – 15 | $W/V_{\rm e}\sin i$ | 0.05 – 0.1 |
| $m$ | $-\ell$ – $\ell$ | $(\delta T/T)_{\rm max}$ | 0.0 – 0.1 |
| $i$ | 25° – 90° | $\alpha_{W_{\rm E}}$ | −4.0 – 2.0 |

**Table 2.** Simulation 2. Same as Table 1 but for a sample allowing for small additional surface-velocity fields

| | | | |
|---|---|---|---|
| $\ell$ | 0 – 15 | $\log k^{(0)}$ | −2.0 – 0.5 |
| $m$ | $-\ell$ – $\ell$ | $\Omega/\omega^{(0)}$ | 0.025 – 0.35 |
| $i$ | 25° – 90° | $(\delta T/T)_{\rm max}$ | 0.0 – 0.1 |
| $W/V_{\rm e}\sin i$ | 0.05 – 0.1 | $\chi^{\rm na}$ | −45° – 45° |
| $V_{\rm max}/V_{\rm e}\sin i$ | 0.00 – 0.01 | $\alpha_{W_{\rm E}}$ | −4.0 – 2.0 |

We performed two Monte-Carlo simulations of the IPS phase diagrams similar to our approach in Paper II. In simulation 1 we calculate the variability due to pulsationally induced $T$-effects only. In simulation 2 we allow for relatively small contributions from a surface-velocity field corresponding to the pulsation.

In simulation 1 the velocity field of the oscillation has zero amplitude in all cases. The values of $k^{(0)}$ and $\Omega/\omega^{(0)}$ are therefore not relevant for the line-profile variability. There is also no need to include the phase lags $\chi^{\rm a}_{k,\ell}$ and $\chi^{\rm na}$, because these parameters determine only the phase differences between the $T$-effects and $V$-effects. Since the above 4 parameters become irrelevant for zero velocity amplitudes, we do not include them in simulation 1.

We computed 60 time series of line profiles for each combination of $\ell$ and $m$ with $\ell\leq$15. The other relevant parameters ($i$, $W$, $(\delta T/T)_{\rm max}$, $\alpha_{W_{\rm E}}$, and for simulation 2 also $V_{\rm max}$, $k^{(0)}$, $\Omega/\omega^{(0)}$, $\chi^{\rm na}$) are chosen at random within the ranges specified in Tables 1 and 2. Values for the inclination are drawn according to the probability $p(i) = \sin i$. In simulation 2 the value for $\log(k^{(0)})$ is drawn such that the combination of $k^{(0)}$ and $\Omega/\omega^{(0)}$ corresponds to an equatorial velocity of less than 50% of break-up. All other parameters are drawn from a flat distribution. For these 15360 time series we derive the absolute blue-to-red phase differences $|\Delta\Psi_0|$ and $|\Delta\Psi_1|$.

To quantify the relations between $|\Delta\Psi_0|$ and $\ell$ and $|\Delta\Psi_1|$ and $m$ we performed least-squares fits of a straight line to the data, assuming linear relations in the ($\ell$,$|\Delta\Psi_0|$) and ($|m|$,$|\Delta\Psi_1|$) planes:

$$\ell = p_\ell + q_\ell|\Delta\Psi_0|/\pi\ ,\ \ |m| = p_m + q_m|\Delta\Psi_1|/\pi\ . \qquad (8)$$

We use an iterative rejection algorithm (sigma-clipping) to discard the outlying points. After the rejection iterations we iteratively increase the number of fit points $N_{\rm fit}$ to all modes within $3\sigma$ distance from the fit, where we estimate $\sigma^2$ as the sum of the squared distances from the fit divided by $N_{\rm fit}$. Finally we record how many modes lie within the intervals [$\ell-1$,$\ell+1$], [$\ell-2$,$\ell+2$],

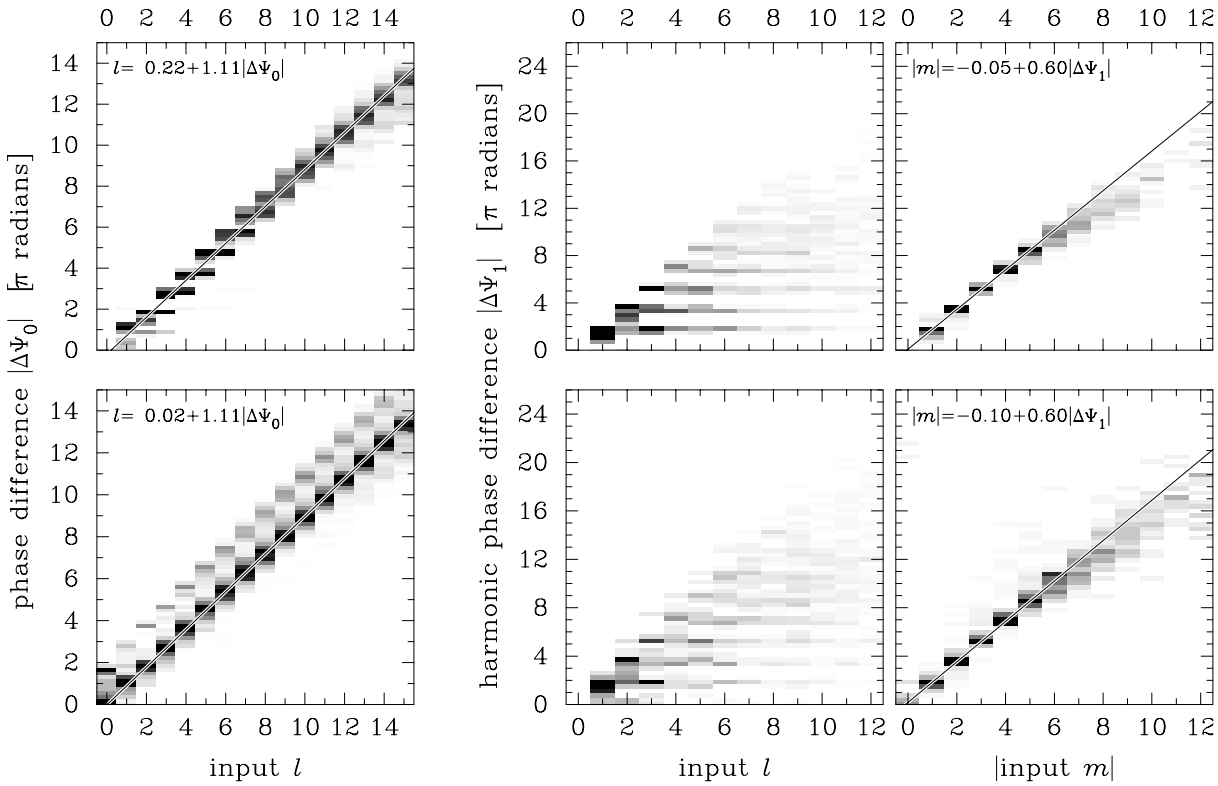


**Fig. 4.** Results of the Monte-Carlo calculations for line-profile variations dominated by $T$-effects. For selections of the computed modes in both samples (see Tables 1 and 2) we plot the blue-to-red phase difference $|\Delta\Psi_0|$ against $\ell$ and $|\Delta\Psi_1|$ against $\ell$ and $|m|$, with the number of occurrences as a grey value. For each vertical bin in the plots the grey scale is normalized to the total number of computed modes in that bin. *Top:* Modes with stellar and pulsation parameters as specified in Table 1 (simulation 1). Only the "detectable" (see Sect. 5.1) modes without slope reversals outside the interval $[-0.25V_{\rm e}\sin i, 0.25V_{\rm e}\sin i]$ (see text below) are used. *Bottom:* Same as top figure, but for the sample specified in Table 2 (simulation 2)

$[\ell-3,\ell+3]$ from the fit (and similar for $|m|$), to estimate the probability that the fit can successfully model real data. We use all modes with $\ell \leq 15$ to fit the coefficients $p_\ell$ and $q_\ell$. To derive the coefficients $p_m$ and $q_m$, we use modes with $\ell \leq 12$.

In addition, to increase the probability to retrieve the correct value of $\ell$ from $\Delta\Psi_0$, we use a subset of modes that excludes the phase diagrams with slope reversals in $\Psi_0(V)$. Slope reversals arise if $\Psi_0(V)$ is not a monotonic function of wavelength/velocity. Phase diagrams with slope reversals do not obey the relation between $\ell$ and $\Delta\Psi_0$ if the reversals are positioned outside the region $[-0.25V_{\rm e}\sin i, 0.25V_{\rm e}\sin i]$. Because such cases can easily be recognized as deviating, it is useful to calculate statistics for the subset without slope reversals outside $[-0.25V_{\rm e}\sin i, 0.25V_{\rm e}\sin i]$. For a detailed discussion and examples of slope reversals in IPS phase diagrams, see Sect. 4.3 of Paper II.

Examples of the results of the Monte-Carlo calculations are given in Fig. 4: for a few selections of all computed modes we plot $|\Delta\Psi_0|$ against $\ell$, and $|\Delta\Psi_1|$ against both $\ell$ and $|m|$, with the number of occurrences displayed as a grey value. For each vertical bin in the plots the grey scale is normalized to the total number of computed modes in that bin.

### *5.1. Cases with variability from only $T$-effects*

Throughout this paper we refer to a class of "detectable" modes, where we excluded all cases which are unlikely to be detectable with present astronomical techniques. We have chosen as an arbitrary condition: $A_{0,1} > 0.001 d_{\rm mean}$. Note that many cases in this class will still be difficult to detect with modern high S/N observations. It is not possible to state a priori what S/N would be required to detect our "detectable" modes, because the number of spectra in the dataset is an important factor.

For only $T$-effects the top panel of Fig. 4 shows a semi-empirical relation between the observable $|\Delta\Psi_0|$ and the index $\ell$ of all "detectable" cases without slope reversals outside $[-0.25V_{\rm e}\sin i, 0.25V_{\rm e}\sin i]$, revealing a very strong correlation between the two. Compared to the similar plot in our Paper II, (Fig 9), the present plot is even less scattered and yields therefore a lower uncertainty in the retrieval of $\ell$. This is evident from the statistics presented in Table 3. If we compare, for example, the entries for 'all modes' in Paper II with our present calculations, we see that for pure $T$-effects the determination of $\ell \pm 1$ has a $93\%$ certainty against $78\%$ for the velocity-dominated modes in Paper II.

**Table 3.** Results for Monte-Carlo simulations for the sample with $T$-perturbations only (see Table 1). For the meaning of "detectable", see our definition in Sect. 5.1. *Top:* Straight line fits to $\ell$ as a function of $|\Delta\Psi_0|$. $N_{\rm tot}$ is the number of modes before rejection. $N_{\rm fit}$ is the number of modes within $3\sigma$ distance from the fit. The rightmost three columns list the percentage of $N_{\rm tot}$ modes that lie within the indicated intervals around the fit. *Bottom:* Straight line fits to $|m|$ as a function of $|\Delta\Psi_1|$

| | $p_\ell$ | $q_\ell$ | $N_{\rm tot}$ | $N_{\rm fit}$ | [$\ell-1$,$\ell+1$] | [$\ell-2$,$\ell+2$] | [$\ell-3$,$\ell+3$] |
|---|---|---|---|---|---|---|---|
| all modes | 0.288(24) | 1.108(3) | 15360 | 13027 | 81% | 89% | 93% |
| "detectable" modes | 0.261(25) | 1.107(3) | 13257 | 12168 | 89% | 95% | 97% |
| modes without slope reversals in $\Psi_0(\lambda)$ outside $[-0.25,0.25]V_{\rm e}\sin i$: | | | | | | | |
| all modes | 0.243(26) | 1.112(3) | 14244 | 12746 | 86% | 94% | 98% |
| "detectable" modes | 0.220(26) | 1.111(3) | 12532 | 11966 | 93% | 99% | 100% |

| | $p_m$ | $q_m$ | $N_{\rm tot}$ | $N_{\rm fit}$ | [$\lvert m\rvert-1$, $\lvert m\rvert+1$] | [$\lvert m\rvert-2$, $\lvert m\rvert+2$] | [$\lvert m\rvert-3$, $\lvert m\rvert+3$] |
|---|---|---|---|---|---|---|---|
| all modes | 1.313(18) | 0.498(2) | 9288 | 9055 | 42% | 83% | 90% |
| "detectable" modes | $-0.047(72)$ | 0.597(12) | 960 | 801 | 95% | 99% | 100% |

**Table 4.** As in Table 3 but for the sample with small additional surface-velocity fields (see Table 2)

| | $p_\ell$ | $q_\ell$ | $N_{\rm tot}$ | $N_{\rm fit}$ | [$\ell-1$,$\ell+1$] | [$\ell-2$,$\ell+2$] | [$\ell-3$,$\ell+3$] |
|---|---|---|---|---|---|---|---|
| all modes | 0.567(23) | 1.037(2) | 15360 | 14609 | 67% | 85% | 95% |
| "detectable" modes | 0.186(26) | 1.096(3) | 13569 | 10575 | 73% | 86% | 98% |
| modes without slope reversals in $\Psi_0(\lambda)$ outside $[-0.25,0.25]V_{\rm e}\sin i$: | | | | | | | |
| all modes | 0.047(30) | 1.111(3) | 13304 | 10020 | 71% | 85% | 98% |
| "detectable" modes | 0.024(30) | 1.112(3) | 12041 | 9317 | 75% | 87% | 100% |

| | $p_m$ | $q_m$ | $N_{\rm tot}$ | $N_{\rm fit}$ | [$\lvert m\rvert-1$, $\lvert m\rvert+1$] | [$\lvert m\rvert-2$, $\lvert m\rvert+2$] | [$\lvert m\rvert-3$, $\lvert m\rvert+3$] |
|---|---|---|---|---|---|---|---|
| all modes | 0.619(17) | 0.525(2) | 10140 | 9847 | 56% | 78% | 89% |
| "detectable" modes | $-0.103(66)$ | 0.598(9) | 960 | 832 | 91% | 98% | 99% |

At first sight this seems also true for the relation between $|\Delta\Psi_1|$ and $|m|$. For the detectable harmonic variability we were able to retrieve $|m|\pm1$ with a certainty of $95\%$, against $53\%$ in Paper II. However, the line-profile variability calculated here turns out to be extremely sinusoidal and the amplitudes of the first harmonic are in all 15360 cases very small, and probably difficult to detect in real observations. In spite of total line-profile amplitudes up to 0.175 $d_{\rm mean}$ the harmonic amplitudes were always smaller than 0.009 $d_{\rm mean}$. On the contrary, the harmonic variability found in our previous calculations (Paper II) is up to 2 orders of magnitude larger for the same line-profile amplitudes. This confirms our earlier finding that redistribution of flux by the surface-velocity field is a far better mechanism to produce harmonic variability than $T$-effects are.

A consequence of the nearly sinusoidal variability associated with $T$-effects is that the harmonics cannot be detected if there is no significant contribution from the surface-velocity field. The plot of $|\Delta\Psi_1|$ against $|m|$, and the corresponding group of entries in Table 3, is therefore not usable in practice for the interpretation of observed variations. It serves merely to prove that the relations also exist for cases with only $T$-effects.

### 5.2. *Cases with variability mainly from $T$-effects, but with a small contribution from the pulsational velocity field*

The bottom panel of Fig. 4 shows the semi-empirical relation between the observable $|\Delta\Psi_0|$ and the pulsation degree $\ell$ for the modes with a small additional surface-velocity field. Adding a surface-velocity field causes a second branch in the relation between $|\Delta\Psi_0|$ and $\ell$, which is known to be related to the horizontal motions of modes with a high $k$-value (see Paper II). In spite of the relatively small additional contribution in this sample, the additional branch is fully developed.

We find that $2\pi$ jumps in the phase diagrams appear as soon as the surface-velocity fields contribute to the variability. The $2\pi$ jumps may appear for $g$ modes (see Paper I, Sect. 6.1.2) and/or an EW response with $\alpha_{W_{\rm E}} < -1.8$ (see Sect. 4.3).

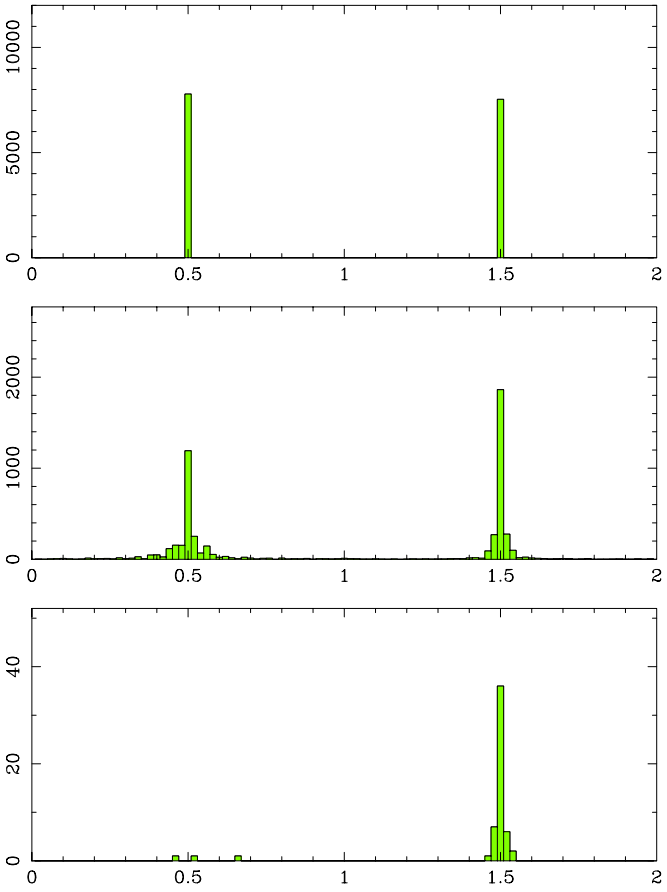

**Fig. 5.** Histogram of the phase difference $\Psi_{01}$=$2\Psi_0-\Psi_1$ at line center, computed for the two samples of 15360 modes. *Top:* Sample with only $T$-effects (see Table 1). *Middle:* Same as top figure, but for the "detectable" subset of the sample which includes small surface-velocity fields (see Table 2) *Bottom:* Same as above, but for the subset with $A_1$>$0.012 d_{\rm mean}$ of the additional sample with surface-velocity fields (Table 2 but with $V_{\rm max}/V_{\rm e}\sin i$ up to 0.02)

We note that small additional surface-velocity fields cause an increased scatter in the relation between $|\Delta\Psi_0|$ and $\ell$ (see Fig. 4 and Table 4).

### 5.3. *Line-center phases at the apparent frequency and at its harmonic*

In Paper II we found that the phase difference between the line center phases $\Psi_0$ and $\Psi_1$, written as

$$\Psi_{01} = 2\Psi_0 - \Psi_1, \qquad (9)$$

is invariant for a translation in time, provided that the observed harmonic frequency is exactly twice the observed frequency $\omega_{\rm obs}$. For the 15360 time series of Paper II we found $\Psi_{01}$=$1.50\pi$ $\pm0.06\pi$, hardly depending on any of the free parameters. This result can be useful to verify that variations detected at $\omega_{\rm obs}$ and $2\omega_{\rm obs}$ arise from the same pulsation mode.

Here we repeat this approach for the two Monte-Carlo simulations specified in Tables 1 and 2. For the sample with only $T$-effects we find in contrast to Paper II, that $\Psi_{01}$ is equally distributed between $\Psi_{01}$=$0.50\pi$ and $\Psi_{01}$=$1.50\pi$. This is illustrated in Fig. 5. For only $T$-effects we find that the response of the local EW $\alpha_{W_{\rm E}}$ is the crucial parameter that determines the value of $\Psi_{01}$. All cases with a positive value for $\alpha_{W_{\rm E}}$ lead to $\Psi_{01}$=$1.50\pi$, whereas the cases with a negative response $\alpha_{W_{\rm E}}$ give rise to $\Psi_{01}$=$0.50\pi$.

Our second sample, with small additional surface-velocity fields (simulation 2), again gives rise to values of $\Psi_{01}$ close to either $\Psi_{01}$=$0.50\pi$ or $\Psi_{01}$=$1.50\pi$, but the small additional $V$-effects tend to transfer cases with a negative value of $\alpha_{W_{\rm E}}$ from $\Psi_{01}$=$0.50\pi$ to $\Psi_{01}$=$1.50\pi$ (see Fig. 5).

Note again that both samples give rise to harmonic variability that is unlikely to be detectable in practice and that our derivation of $\Psi_{01}$ in these cases is only possible due to the absence of noise in our theoretical spectra.

From simulations 1 and 2 we find that an increase of the $V$-effects leads to an increased amplitude of the harmonic variations as well as an increased trend towards $\Psi_{01}$=$1.50\pi$. This raises the important question whether at a certain detection limit, all cases with a "detectable" harmonic will be transferred to $\Psi_{01}$=$1.50\pi$. Because our sample with small $V$-effects contains only few cases with detectable harmonic variability, we performed an additional Monte-Carlo simulation in which we allowed twice as large surface-velocity fields as in simulation 2. This third simulation is suitable to investigate the above question because it contained a sufficient amount of cases (9589) with a "detectable" harmonic, distributed between $A_1 = 0.001$ $d_{\rm mean}$ and $A_1 = 0.033$ $d_{\rm mean}$.

As expected, the variability calculated in the third simulation confirms that the peak around $\Psi_{01}$=$0.50\pi$ disappears completely if the surface-velocity contributions to the line-profile variability are large enough. We find that for harmonic amplitudes $A_1$ larger than 0.012 $d_{\rm mean}$ all systematic effects leading to $\Psi_{01}\approx0.50\pi$ have disappeared.

In Paper II we concluded that a measurement of $\Psi_{01}\approx1.50\pi$ confirms that the main frequency and its harmonic are caused by NRP. The present results show that only in data sets of an extremely high quality (S/N, time span and time coverage), cases with $\Psi_{01}\approx0.50\pi$ may be detected. Therefore, we confirm that in practice our conclusion of Paper II is also valid for line-profile variations that are dominated by temperature effects of NRP.

## 6. Conclusions

The main conclusions of this paper can be summarized as follows.

1. The characteristics which distinguish between low and high $k$-values, may disappear completely if local brightness and EW variations dominate the line-profile variability. We confirm that the double-peaked amplitude distributions of $g$ modes may turn into a concave distribution typical for $p$ modes. Reversely, we find cases in which the rectangularly shaped amplitude distribution mode becomes double-peaked.
2. In specific lines the local brightness variations will cancel the local EW variations. Such cancellation effects might lead to underestimated surface-temperature variations.

3. Asymmetric amplitude distributions are typical for cases in which both $V$-effects and $T$-effects contribute significantly to the line-profile variability, provided that the pulsation is non-adiabatic. The centroid of the asymmetric distribution is determined by the sign of the non-adiabatic phase lag and by the relative responses of the local EW and brightness, with $p$ and $g$ modes behaving oppositely.
4. Harmonic variability is a characteristic of line-profile variability arising from surface-velocity variations. The existence of harmonic variability depends on the contribution of the surface-velocity field to the line-profile variations. In spite of amplitudes $(\delta T/T)_{\max}$ up to $10\%$ and line-profile amplitudes up to 0.175 $d_{\mathrm{mean}}$ our sample with only $T$-perturbations shows extremely small harmonic amplitudes which are not detectable by the present observational techniques. This is different from equally large line-profile variations arising from surface velocities, for which harmonic variability is a rule rather than an exception.
5. The amplitude of the harmonic relative to the amplitude found at the main frequency provides information about the relative contributions of velocity fields and temperature perturbations to the line-profile variations.
6. The IPS phase diagrams are not very sensitive to the particular mechanism by which the line-profile variability originates. The determination of the $\ell$ and $|m|$ values of a pulsation mode from observed time-series of line profiles can be achieved without knowledge about the dominant mechanism. This is convenient because the parameters which determine the $T$-perturbation need not to be known to retrieve $\ell$ and $m$.

*Acknowledgements.* We thank Huib Henrichs for his supportive remarks and careful reading of the manuscript.

## References

Aerts C., Waelkens C., 1993, A&A, 273, 135
Baade D., 1984, A&A, 135, 101
Balona L.A., 1987, MNRAS, 224, 41
Buta R.J., Smith M.A., 1979, ApJ, 232, 213
Cugier H., Dziembowski W.A., Pamyatnykh A.A., 1994, A&A, 291, 143
Gies D.R. 1991, In: Baade (ed.) Rapid Variability of OB stars. ESO Proc. 36, p. 299
Gies D.R., Kullavanijaya A., 1988, ApJ, 326, 813
Hao J., 1998, ApJ, 500, 440
Kambe E., Ando H., Hirata R., 1990, PASJ, 42, 687
Kambe E., Osaki Y., 1988, PASJ, 40, 313
Kennelly E.J., Walker G.A.H., Merryfield W.J., 1992, ApJ, 400, L71
Kurucz R.L., 1992, In: Barbuy B., Renzini A. (eds.) The Stellar Populations of Galaxies. Proceedings of IAU Symposium 149, p. 225
Lee U., Jeffery C.S., Saio H., 1992, MNRAS, 254, 185
Saio H., Cox J.P., 1980, ApJ, 236, 549
Schrijvers C., Telting J.H., Aerts C., Ruymaekers E., Henrichs H.F., 1997, A&AS, 121, 343 (Paper I)
Smith M.A., 1977, ApJ, 215, 574
Stellingwerf R.F., 1978, AJ, 83, 1184
Telting J.H., Schrijvers C., 1997, A&A, 317, 723 (Paper II)
Telting J.H., Schrijvers C., 1998, A&A, (accepted)
Townsend R.H.D., 1997, MNRAS, 284, 839
Vogt S.S., Penrod G.D., 1983, ApJ, 275, 661
Wade R.A., Rucinski S.M., 1985, A&AS, 60, 471